https://doi.org/10.5194/egusphere-2026-2617
Preprint. Discussion started: 11 June 2026

Classification and quantification of low-visibility events using deep learning over eastern China

Yuting Liang[1], Shitong Zhao[1], Dantong Liu[1*], Changhao Wu[1,2,3], Li Yi[4], Xingcan Jia[5]

[1]School of Earth Sciences, Zhejiang University, Hangzhou, China

[2]Yunnan University, Kunming, China

[3]Yunnan International Joint Laboratory of Monsoon and Extreme Climate Disasters, Kunming, China

[4]Ocean University of China, Qingdao, China

[5]Institute of Urban Meteorology (IUM), Chinese Meteorological Administration, Beijing, China

Correspondence to: Dantong Liu (dantongliu@zju.edu.cn)

Abstract

Low-visibility events (LVEs) threaten transportation safety and human health, yet accurately identifying them at a regional scale remains challenging. To address this, this study introduces a unified convolutional neural network (CNN) framework that integrates the geostationary satellite, meteorology, and fine particulate matter ($PM_{2.5}$) observation data to identify all types of LVEs. The model can not only produce the spatiotemporal distribution of LVEs, including land and sea fog, but also quantify the intensity of LVEs linked to visibility reduction. By incorporating $PM_{2.5}$, the polluted fog-haze over land can be discriminated from clean fog. Based on the model, we are able to investigate the environmental policy to reduce fog-haze and the corresponding population exposure. Over eastern China, a 20% reduction of overall $PM_{2.5}$ can reduce the fog-haze area by 42% in winter. However, the corresponding population exposure is reduced less effectively by 15%, because the most populated region collocates with the most polluted region, where a further reduction of $PM_{2.5}$ by over 40% is required to effectively reduce its population exposure. Here, the classified and quantified LVEs, along with the established relationship with pollution, explicitly guide the air-quality policy for the co-benefits of improving air visibility and human health.

Keywords: Deep Learning, Satellite Remote Sensing, $PM_{2.5}$, Low-Visibility Events, Sensitivity Analysis, Population Exposure

https://doi.org/10.5194/egusphere-2026-2617
Preprint. Discussion started: 11 June 2026

1 Introduction

Low-visibility events (LVEs) are pervasive atmospheric phenomena occurring across both terrestrial and marine environments. Broadly categorized into fog, haze, and their mixture (fog-haze), these events degrade atmospheric transparency through light extinction by suspended liquid droplets and fine particulate matter, directly impacting transportation safety ((Ord Us Epa, 2015; Oar Us Epa, 2015; An et al., 2019). Fog results from the cloud condensation nuclei (CCN) when moisture is sufficient to activate aerosols as droplets (Gultepe et al., 2007). The microphysical properties of droplets, including the size spectrum and relative dispersion, can be influenced by aerosol concentration (Twomey, 1977a; Liu and Daum, 2002). The amount of aerosols contained in fogs can also determine the pollution level of fogs, as a polluted fog containing high aerosol loadings (i.e., the fog-haze) can exert adverse health impacts (Zhang et al., 2014). Identifying different types of LVEs is important to understand their impacts and to make effective environmental policies.

Remote sensing of satellites provides a powerful tool to identify fogs from complex cloud types on a broad spatial scale (Gultepe et al., 2007; Cermak and Bendix, 2008). The threshold methods from certain or multiple parameters have been conventionally used to identify fog events (Ellrod, 1995; Eyre et al., 1984). For instance, nighttime fog is typically detected utilizing the brightness temperature difference (BTD) between infrared channels (Eyre et al., 1984; Hunt, 1972). For daytime detection, the algorithm utilizes visible and 3.9 μm shortwave infrared reflectance to distinguish water clouds from snow and ice (Lee et al., 1997; Anthis and Cracknell, 1999). Additionally, textural thresholds distinguish smooth fog from rough clouds (Wu et al., 2015), and the temperature difference between the cloud top and sea surface confirms low-level fog (Zhang and Yi, 2013). Machine learning and sometimes deep learning methods have recently widely developed to learn the nonlinear relationships from data, which improve the performance beyond the fixed threshold method (Huang et al., 2022; Jeon et al., 2020; Shin and Kim, 2018). The generalization of models can be improved by incorporating large-scale multi-source data (Xu et al., 2025). The dense haze could be misclassified as cloud due to its similar reflective properties (Hutchison et al., 2008). Furthermore, regarding the distinction between polluted and unpolluted fog, although studies have noted microphysical differences, including a smaller droplet effective radius in polluted environments (Mazoyer et al., 2019), operational methods to explicitly identify the polluted fogs remain scarce. Given these detection challenges, few studies have simultaneously identified all LVE types, including land and sea fog as well as unpolluted and polluted fog, thereby studying their potential interaction and conversion.

In this study, we develop a multi-source fusion model based on a convolutional neural network (CNN) to identify all types of LVEs over land and sea. This model integrates the satellite spectral data with the meteorology reanalysis and ground $PM_{2.5}$ observations. By systematically altering $PM_{2.5}$ concentrations in the model, we quantify the impact of pollution abatement on winter fog-haze to guide the cost-effective air quality policy.

2 Data and Observations

2.1 Study Region

The study focuses on eastern China (Fig. S1), a region characterized by a monsoon climate, dense population, and intense anthropogenic emissions (Zhang et al., 2009a; Li et al., 2017). This region frequently experiences interactions between marine moisture and anthropogenic aerosols, generating all types of LVEs, including land and sea fog as well as polluted and unpolluted fog (Niu et al., 2010)

2.2 Multi-source Observational Datasets

We constructed a multisource dataset for 2019 to 2020 by integrating geostationary satellite observations, meteorological reanalysis, air quality measurements, and ground based visibility observations (Table S1). Satellite inputs were obtained from FY-4A and included brightness temperatures (BT) at 3.72 and 10.8 micrometers, together with solar zenith angle (SOZ) (Yang et al., 2017). The 10.8 micrometer thermal infrared channel provides information on cloud top temperature, effectively separating low-level fog from colder, elevated cloud layers (Cermak and Bendix, 2008). The 3.72 μm shortwave infrared channel distinguishes fine haze from fog, as only the larger fog droplets trigger strong Mie scattering, while haze interacts weakly (Gultepe et al., 2007). The brightness temperature difference between these two channels (BTD, $BT_{3.72} - BT_{10.8}$) enhances the spectral contrast among fog, haze, and the background (Hunt, 1972). Solar zenith angle was included to account for variations in illumination during the diurnal cycle (Wei et al., 2021).

Meteorological variables were obtained from ERA5 reanalysis, including 2 m temperature and 2 m dew point temperature (Hersbach et al., 2020). The temperature and dew point spread was used as a proxy for near surface saturation and helped distinguish ground contacting fog from unsaturated low stratus or aerosol dominated haze (Pauli et al., 2020). Hourly $PM_{2.5}$ concentrations were obtained from the China National Environmental Monitoring Centre (CNEMC) and used to represent aerosol loading over land. Hourly ground based visibility observations were obtained from the NOAA/NCDC Integrated Surface Database Lite (ISD-Lite) and used as the observational basis for LVE labelling. Population data at 1 km resolution were obtained from WorldPop and used only for the population exposure analysis.

2.3 Visibility Definition and LVE Labelling

In this study, visibility (Vis) refers to the near-surface horizontal meteorological optical range, namely the distance over which the contrast of an object against the background is reduced to a threshold perceptible to a human observer (WMO, 2024). Physically, for the fog- and haze-related LVEs targeted here, Vis is governed primarily by atmospheric extinction caused by scattering and absorption by fog droplets and aerosol particles. Following the Koschmieder relationship, Vis can be related to the atmospheric extinction coefficient β_{ext} as Vis = 3.912 / β_{ext} (Koschmieder, 1924; Israël and Kasten, 1959). Therefore, a reduction in Vis indicates enhanced near-surface optical extinction.

The occurrence of LVEs was defined using ground measured visibility. Station observations with Vis <= 2 km were labelled as low visibility, while observations with Vis > 2 km were labelled as clear (Lyu et al., 2021). The station level labels were then mapped to the nearest 4 km FY-4A grid cell to generate a binary mask for model training and validation. The CNN was trained on this binary mask to detect low visibility, while event types were assigned after prediction using temperature dew point spread and $PM_{2.5}$ (Sect. 3.1).

2.4 Data collocation and preprocessing

All datasets were temporally matched to the hourly visibility observations and spatially resampled to the 4-km FY-4A grid. ERA5 variables and station-based $PM_{2.5}$ and visibility observations were interpolated or assigned to the satellite grid, and missing values were filled using nearest-neighbour interpolation. The collocated variables were then cropped into 64 x 64 pixel windows for CNN training and prediction, as illustrated in Fig. 1. Further details of data preprocessing and standardization are provided in Text S1.

3 Methodology

3.1 Overall framework and physical attribution

The overall framework for identifying and attributing low-visibility events (LVEs) is illustrated in Fig. 1. Ground-based visibility observations were used to generate the binary low-visibility mask for model training. Multisource satellite, meteorological, and $PM_{2.5}$ fields were collocated on the FY-4A grid and processed using a window-sampling strategy. The model output identifies low-visibility pixels, which were subsequently assigned to event types using physically interpretable environmental criteria.

Over land, identified low-visibility pixels were attributed using dew point depression as a proxy for near-surface saturation and $PM_{2.5}$ as a proxy for aerosol loading. Pixels were classified as fog when dew point depression was < 3 °C and $PM_{2.5}$ was < 75 µg m^{-3}, as fog-haze when dew point depression was < 3 °C and $PM_{2.5}$ was ≥ 75 µg m^{-3}, and as haze when dew point depression was ≥ 3 °C and $PM_{2.5}$ was ≥ 75 µg m^{-3}. The humidity criterion reflects fog-favourable near-surface saturation (Pauli et al., 2020), while the $PM_{2.5}$ threshold follows the Grade-II 24 h limit of the Chinese Ambient Air Quality Standard (GB 3095-2012). Over ocean grids, low-visibility pixels from the Sat model were attributed to sea fog. This post-processing scheme separates the optical occurrence of low visibility from its likely physical cause.

Weak precipitation, drizzle, and fog often co-occur in the real atmosphere and jointly affect near-surface extinction. Pronounced low visibility is more closely associated with drizzle-fog mixed conditions than with rain-only cases, while rain-only cases without fog generally do not produce the LVEs targeted here (Wang et al., 2021). We therefore did not subdivide LVEs by precipitation occurrence.

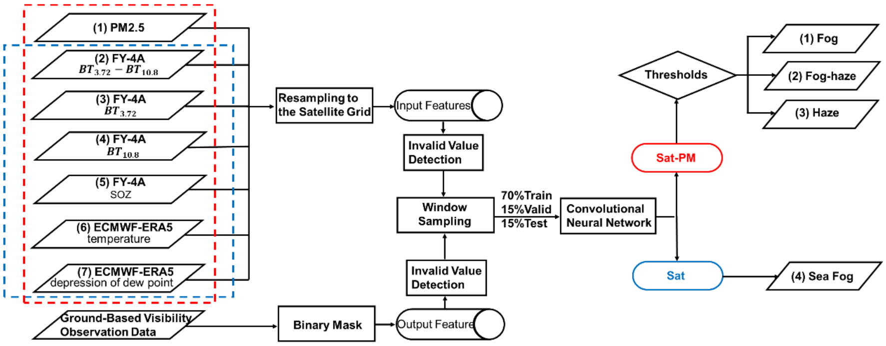

Figure 1. Schematic of the analytical framework. The blocks from left to right are the input and output parameters, the procedures of dataset preparation for the machine learning, and the model outputs. The ground visibility observations are processed into a binary mask to serve as

the output for model training. The framework utilizes the convolutional neural network (CNN) to output the map of low-visibility events over land, including fog, fog-haze, and haze, using the satellite and $PM_{2.5}$ data (the SAT-PM model), and the sea fog using the satellite data only (the SAT model).

3.2 Model configuration to classify LVEs

The identification framework employs a CNN architecture to map the multi-source input tensors (dimensions of $C \times 64 \times 64$, where C represents variable channels) to event probabilities. As detailed in Fig. S2 and Text S2, the feature extraction module consists of three sequential convolutional blocks. Each block comprises a 3×3 convolutional layer to capture local spectral-spatial patterns, followed by batch normalization (BatchNorm) (Ioffe and Szegedy, 2015) and rectified linear unit (ReLU) activation (Krizhevsky et al., 2012) to ensure training stability. A max-pooling layer concludes each block, progressively reducing spatial resolution from 64×64 to 8×8 while expanding feature depth from 32 to 128 channels. The high-dimensional features are subsequently flattened and processed by two fully connected layers, reducing dimensionality from 8,192 to 512, before the final Softmax activation yields the probability scores for low-visibility and clear classes.

To address the feature redundancy inherent in multi-source data and the spatial heterogeneity of the background, a dual-branch attention mechanism is embedded within the convolutional blocks. The variable-wise attention module utilizes global average pooling to compute importance weights for each input channel, allowing the model to adaptively prioritize the most informative channels while suppressing noise (Hu et al., 2018). Simultaneously, the spatial attention module employs a 7×7 convolution kernel to focus on informative regions, effectively distinguishing fog boundaries from complex underlying surfaces (Woo et al., 2018).

Training is driven by a hybrid loss function designed to overcome the class imbalance between rare LVEs and frequent clear conditions. This function combines balanced focal loss and dice loss with equal weighting (Lin et al., 2017; Milletari et al., 2016). The focal loss down-weights easy negatives by setting a focusing parameter $\gamma = 3.0$ and a balancing coefficient $\alpha = 0.55$, forcing the model to concentrate on minority samples. Meanwhile, the dice loss optimizes the F1-score, balancing precision and recall to ensure identification performance even when low visibility samples are rare. Detailed mathematical formulations and tensor transformations are provided in Text S2 and Text S3.

3.3 Model Training and Validation

The final dataset comprises 1,440 LVEs observed during 2019–2020. A partition-then-sample strategy is introduced to divide events into training (70%), validation (15%), and test (15%) subsets, followed by spatial samples extraction using non-overlapping sliding windows (142 km × 142 km) as shown in Fig. S1b Using ground-based observations as the ground truth, two model variants were trained: the land-based Sat-PM model, which incorporates $PM_{2.5}$ concentrations to separate clean from polluted low-visibility events, and the maritime Sat model, which excludes this input due to minimal anthropogenic influence over open oceans. The models were optimized using the AdamW algorithm with dynamic learning rate scheduling and early stopping mechanisms to ensure stable convergence. Furthermore, a progressive dropout strategy was applied to the fully connected layers to enhance generalization and prevent overfitting. Detailed training hyperparameters and regularization strategies are documented in Text S4.

3.4 Metrics to quantify LVEs

Three parameters are defined to analyze the model outputs. The LVE intensity (I_{pixel}) is quantified using an overlapping sliding window approach (64×64 pixels with a stride of 8) that traverses the target area. Within each window, the model outputs a binary classification (low-visibility=1 or clear=0). The final intensity for a given pixel is defined as the ratio of positive classifications to the total number of overlapping windows covering that pixel. This can be expressed as:

$$I_{\text{pixel}} = \frac{\sum_{i=1}^{N} C_{\text{i}}}{N_{\text{total}}} \quad (1)$$

where I_{pixel} denotes pixel intensity, N_{total} is the overlapping window count, and C_{i} indicates the i-th window status (low-visibility=1 or clear=0).

The LVE area is calculated to characterize the spatial extent of events. This is derived by aggregating all grid pixels identified with positive LVE intensities (I_{pixel}>0) and converting the pixel count into geographical area (km^2) based on the grid resolution.

The population-weighted intensity (PWI), referred to as population exposure, quantifies the average fog-haze intensity experienced by an individual within the study region. The gridded population distribution data were obtained from WorldPop (https://www.worldpop.org/) at a resolution of 1 km. It is calculated by multiplying the fog-haze intensity in each grid cell (I_{i}) by the population in that cell (P_{i}), summing all grids over the entire domain, then dividing by the total domain population, as shown in Eq. (2):

$$PWI = \frac{\sum_{i=1}^{N} (I_{\text{i}} \times P_{\text{i}})}{\sum_{i=1}^{N} P_{\text{i}}} \quad (2)$$

where i is an individual grid cell in the domain, N is the total number of grid cells, I_{i} is the fog-haze intensity in grid cell i, and P_{i} is the population in grid cell i.

4 Results and discussions

4.1 Overall Performance of models

As summarized in Table S2, the terrestrial Sat-PM model demonstrated superior performance on independent test datasets, achieving an overall accuracy of 0.93, an F1-score of 0.78, and a recall of 0.81. In parallel, the maritime Sat model proved robust for sea fog detection, securing an accuracy of 0.91 and a fog-specific F1-score of 0.71. Furthermore, Table S3 demonstrates the model structural advantages and performance superiority over baseline configurations. These results quantitatively confirm that $PM_{2.5}$ is critical for the reliable detection of complex LVEs over land, while affirming the Sat model capability for the sea fog detection task.

4.2 Spatiotemporal distribution and intensity of classified LVEs

Figure 2a shows the input features for LVEs on February 5th-6th, 2019. The Sat-PM model is delineated by the red box, and the Sat model (blue box) operates without $PM_{2.5}$ data. A binary mask derived from ground-based station visibility observations serves as the ground truth (Fig.

https://doi.org/10.5194/egusphere-2026-2617
Preprint. Discussion started: 11 June 2026

2b), where red pixels denote areas classified as low-visibility (visibility ≤ 2 km). The model output, shown in Fig. 2c, effectively discriminates between different types of low-visibility phenomena through a two-step process.

Following the physical attribution scheme described in Sect. 3.1, the Sat model identifies sea fog over ocean grids (Fig. 2c(i)), while the Sat-PM model attributes terrestrial low-visibility pixels to fog, fog-haze, or haze (Fig. 2c(ii)). By integrating the outputs, a synthesized map (Fig. 2c(iii)) provides a comprehensive product that covers both land and sea. In the visualization, color opacity maps directly to the intensity of each phenomenon.

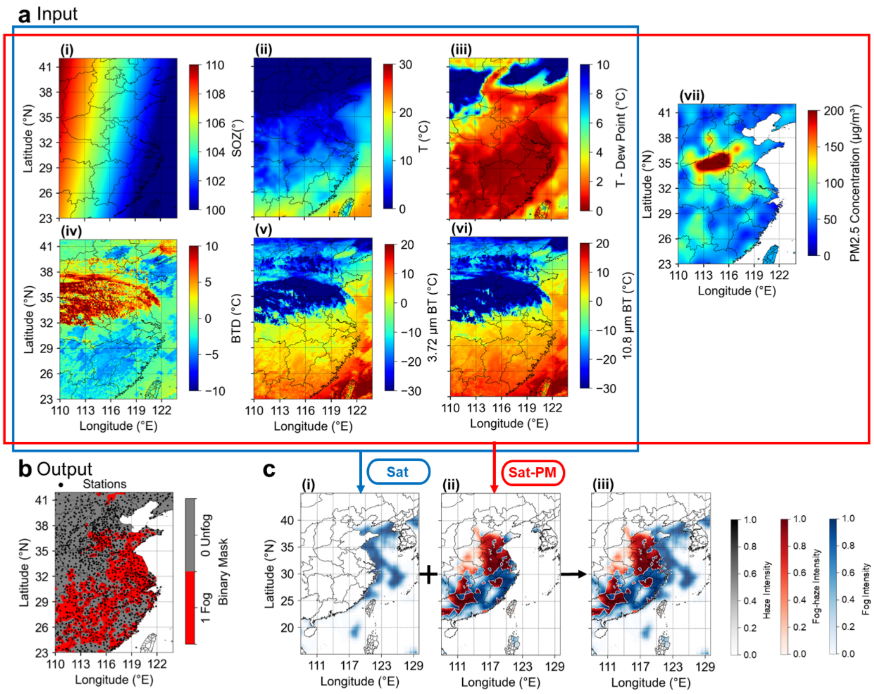

Figure 2. An example of input and output parameters to classify the spatial distribution of low-visibility events. (a) Input parameters, including solar zenith angle (i), temperature (ii), dew point depression (iii), brightness temperature difference (BTD) (iv), brightness temperature (BT) at 3.72 μm (v), BT at 10.8 μm (vi), and $PM_{2.5}$ (vii), are used for the Sat-PM model. (b) The binary mask determined by the ground observation of visibility, with red pixels representing fog (value=1). (c) The intensity maps of identified sea fog by the SAT model (i), fog and fog-haze by the SAT-PM model (ii), and combined results (iii).

Figure 3 illustrates the spatiotemporal evolution of the LVE from 15:00 on Feb. 5th to 15:00 on Feb. 6th. The model results show that the low-visibility region initially formed along the coast and subsequently expanded inland and over the sea, intensifying and reaching its peak extent during the night and early morning. Thereafter, it gradually dissipated, demonstrating the dynamic detection capability of the model for LVEs.

https://doi.org/10.5194/egusphere-2026-2617
Preprint. Discussion started: 11 June 2026

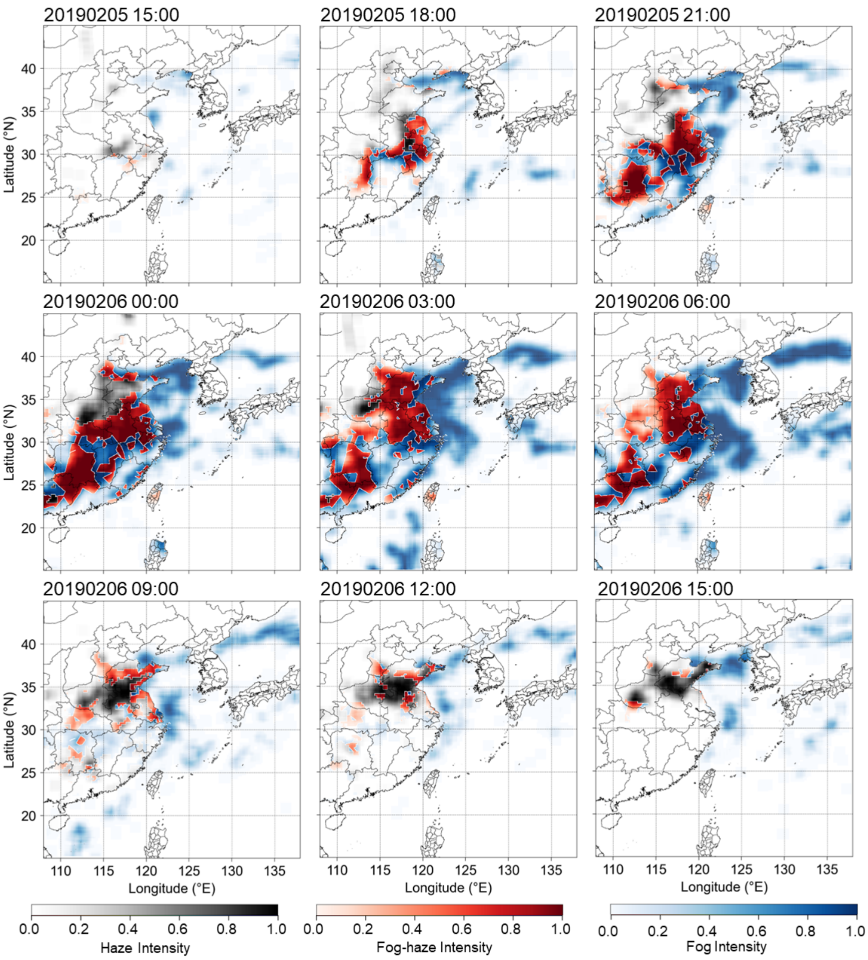

Figure 3. An example of the spatial distribution of low-visibility events with identified fog, fog-haze, haze, and sea-fog in Feb. 2019, all colored by the intensity of classified events.

To further evaluate the model performance, the simulated LVE intensities were compared with the observed visibility from ground stations. Six stations are chosen to validate the land and sea fog, respectively. Figure 4a shows the spatial evolution of a representative fog event on 15 February 2020, together with the locations of the selected validation stations. The model captures the development, displacement and weakening of the fog field during this event.

Figure 4b compares the simulated sea-fog intensity from the Sat model with visibility reduction observed at Dinghai, Putuo and Shengsi. Visibility was expressed as 5 km minus the observed visibility to allow direct comparison with fog intensity. The simulated intensity peaks generally coincide with periods of reduced visibility at the coastal and island stations, yielding a correlation coefficient of r = 0.67. Some model-identified sea-fog periods were not matched by

https://doi.org/10.5194/egusphere-2026-2617
Preprint. Discussion started: 11 June 2026

station observations, accounting for about 16% of the month. This is because the ground observations were not in the central part of the sea fog, where the fog may partly dissipate at the edge, causing incomplete observation. The satellite data may overestimate the fogs by misinterpreting the low-level clouds (Cermak and Bendix, 2008). The identified sea fog here followed reasonable diurnal variations (peaking at night and dissipating in the morning), thus less likely to be a systematic misinterpretation of low-level clouds.

For land LVEs, the Sat-PM model output was validated against Quanjiao, Hanshan and Dangtu (Fig. 4c). The simulated intensity is also consistent with observed visibility reduction, with a correlation coefficient of r = 0.69, and reproduces the onset and dissipation of most land-LVE events. Only about 19% of the period was mismatched. These validations indicate that the model captures not only the spatial distribution of LVEs over land and sea, but its modelled intensity also quantifies the extent of LVEs, which can be linked to visibility.

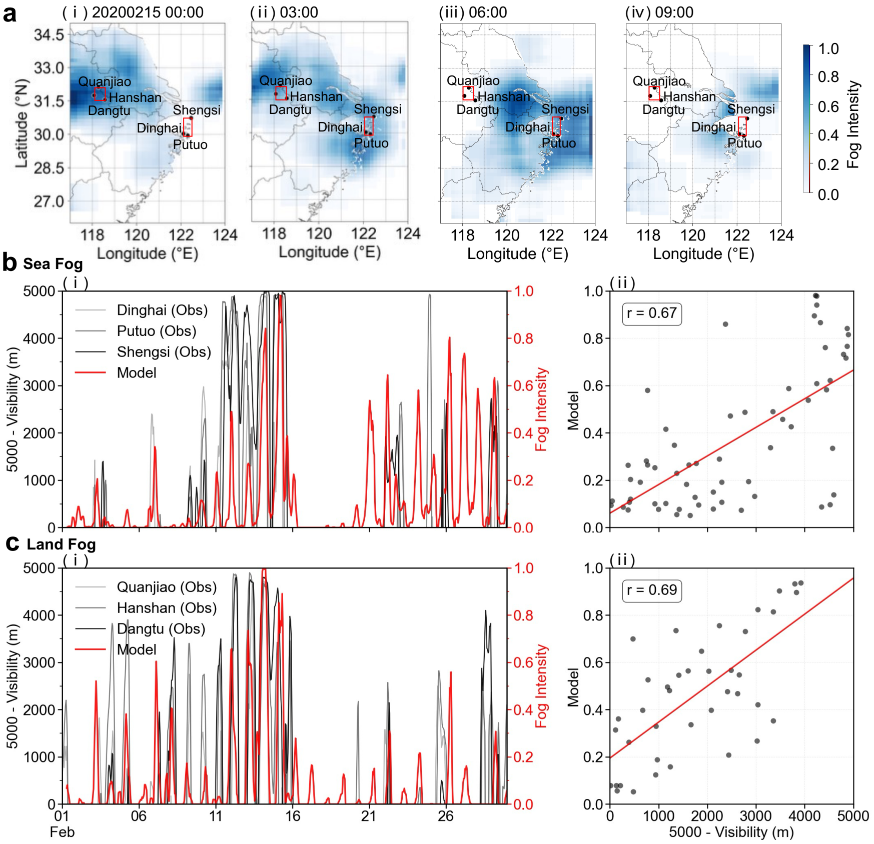

Figure 4. Validation of simulated sea-fog and land-fog intensity at representative coastal and continental stations. (a) Spatiotemporal evolution of a fog event on Feb. 15th, 2020. The model simulation in red squares is compared with the three stations in the square, respectively, for the land and sea-fog. (b) Sea-fog validation. The left panel shows the temporal evolution of station-observed visibility reduction, expressed as 5000 m minus visibility, together with modelled fog

https://doi.org/10.5194/egusphere-2026-2617
Preprint. Discussion started: 11 June 2026

intensity. The right panel shows the corresponding station-collocated scatter plot between observed visibility reduction and modelled fog intensity. (c) Same as b, but for land-fog stations.

4.3 Variability of LVE areas

Besides the LVE intensities, LVE areas are analysed. February and July were selected to represent the meteorological regimes of the cold and warm seasons, respectively. Figure 5a demonstrates that the proposed method effectively distinguishes LVE types and captures their dominant hourly variations. While both winter and summer exhibit distinct diurnal patterns, their coverage magnitudes differ. For sea fog and land fog-haze, the winter dominance is evident in both intensity and extent. Regarding seasonal variations, the wintertime peak median area for sea fog is approximately 1.75 times larger than in summer, while land fog-haze intensity drops to negligible levels in July compared to distinct winter peaks (Fig. 5b(ii) vs. 5c(ii)). Consistent with climatological patterns where haze peaks in winter (Zhang et al., 2012) and sea fog in spring (Zhang et al., 2009b), the total accumulated coverages of winter land fog-haze and sea fog are substantially higher, being approximately 21.0 and 1.8 times those in summer (Fig. 5a(ii) and 5a(iv)). However, land fog exhibits a more complex seasonal characteristic. Regarding the maximum spatial extent, the wintertime peak coverage for land fog exceeds that of summer, reaching approximately 1.5 times the maximum area observed in July (peaking at ~140,000 km² in Fig. 5a(i) vs. ~95,000 km² in Fig. 5a(iii)). This aligns with previous findings that stronger radiative cooling in winter favors extensive fog events (Zhang et al., 2014; Roach et al., 1976). Yet, contrary to the typical autumn-winter peak observed for inland fog (Niu et al., 2010), the total area of land fog remains consistent across the two seasons (Fig. 5a(ii) and 5a(iv)). This discrepancy can be attributed to the coastal nature of the study domain. Although winter land fogs tend to be larger and more intense due to strong cooling, summer compensates with more frequent fog formation driven by abundant moisture, effectively balancing the total coverage.

The diurnal variations of the four LVE types exhibited distinct patterns (Fig. 5b, c). Generally, land-based fog and fog-haze aligned with the diurnal cycle of relative humidity (RH), peaking before dawn and dissipating post-sunrise. This behavior corroborates the mechanism of classic radiation fog, driven by nocturnal radiative cooling and rapid dissipation via solar heating (Roach et al., 1976). However, seasonal heterogeneities were observed. For land fog, the peak coverage occurred later in winter (07:00–08:00) compared to summer (05:00–06:00) (Fig. 5b(i)), primarily attributed to the delayed sunrise and weaker solar radiation in the cold season, which retards the dissipation process. The land fog-haze showed similar start and dissipating time with land fog, but with subustanially larger coverage in winter than summer due to the higher pollution in the cold season (Fig. 5b(ii) and 5c(ii)). The fog-haze had a slightly earlier accumulation time than fog, maybe due to the decreased boundary layer at night, which enhanced the pollution level.

In winter, the area of dry haze peaked during the nocturnal and early morning hours (05:00) (Fig. 5b(iii)). Following sunrise, the development and deepening of the boundary layer enhances vertical mixing and dispersion, leading to a rapid decrease in haze area, which reaches its daily minimum in the afternoon (15:00). While summer showed the minimal haze area

https://doi.org/10.5194/egusphere-2026-2617
Preprint. Discussion started: 11 June 2026

overnight, increasing after sunrise, and peaked from late morning to midday (10:00–13:00). This indicated the summer haze formation was likely driven by photochemical reactions, when intensive daytime solar radiation produced secondary aerosols, overcoming the dilution effect of boundary layer. Previous studies also indicate that $PM_{2.5}$ accumulates at night in winter, while the peak $PM_{2.5}$ concentration occurs during the day in summer (Wu et al., 2024).

The sea fog showed a similar pattern in winter, while the summer sea fog extended longer than winter (Fig. 5c(iv)). This persistence is characteristic of advection fog. In summer, sea fog coverage extended well into the noon, dissipating much more slowly than its land counterpart. This persistence arises because sea fog formation is governed by the cooling of warm, moist air over the colder sea surface rather than the rapid diurnal temperature cycle of the land surface (Koračin et al., 2014). Unlike the land surface, the sea surface temperature (SST) shows a slow diurnal evolution, maintaining a stable marine boundary layer that resists immediate dissipation by solar radiation (Liu et al., 2016).

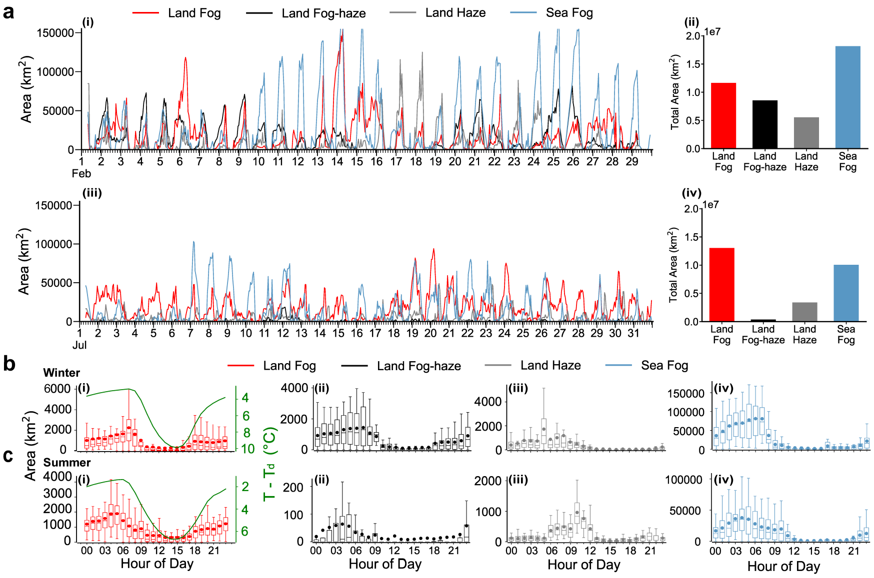

Figure 5. Temporal variations of low-visibility event areas in winter (Feb.) and summer (Jul.). (a) Time series (i, iii) and total accumulated areas (ii, iv) for land fog (red), land fog-haze (black), land haze (grey), and sea fog (blue). (b, c) Diurnal variations of event areas for (i) land fog, (ii) land fog-haze, (iii) land haze, and (iv) sea fog in (b) winter and (c) summer. Green lines in (i) represent the temperature–dewpoint spread ($T – T_d$). Box plots indicate the median (line), mean (dot), interquartile range (box), and data range (whiskers).

4.4 Sensitivity of fog-haze events to $PM_{2.5}$ mitigation

The model established above allows us to quantify the impacts of $PM_{2.5}$ on the formation of fog-haze. The sensitivity experiments are hereby performed by systematically adjusting $PM_{2.5}$ concentration inputs in the validated Sat-PM model. A case study from Feb. 9th, 2020 (Fig. 6a) showed that under original $PM_{2.5}$ levels, the model identifies a large, intense patch of fog-haze (red shading) over land. As $PM_{2.5}$ concentrations progressively reduce to 80%, 60%, and 40%, the model shows the reduced intensity of fog-haze but increased clean fog, indicating the importance of $PM_{2.5}$ in transforming fog into fog-haze. The fog-haze area change corresponding to the $PM_{2.5}$ change for the whole month is shown in Fig. 6c. The baseline simulation (with original $PM_{2.5}$) shows multiple large-scale fog-haze events, with peak area exceeding 70,000 km². A 20% reduction (to 80% original levels) consistently lowered these peaks. More aggressive reduction had a more apparent effect, i.e., reducing emissions to 60% can eliminate most large-scale fog-haze. This confirms that the spatial coverage of fog-haze is highly sensitive to $PM_{2.5}$ levels.

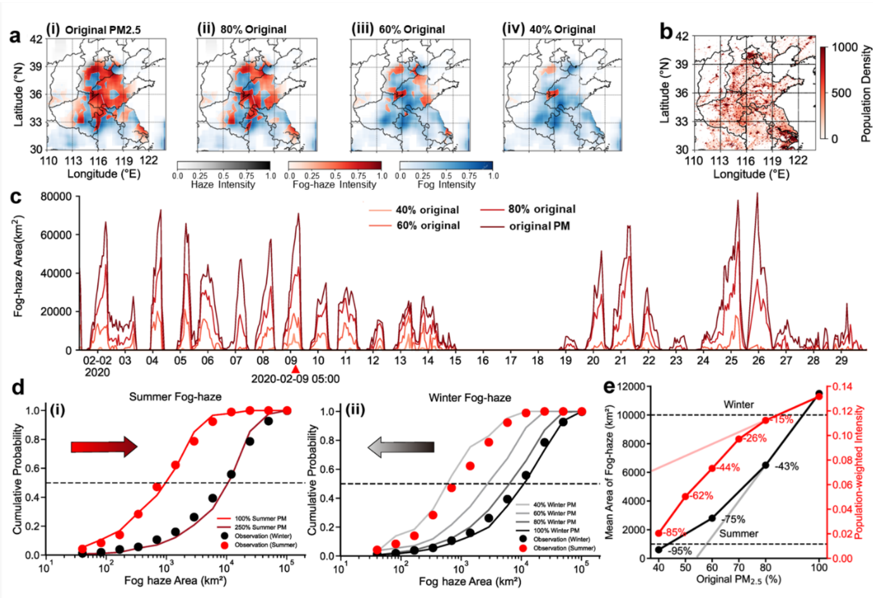

Figure 6. Sensitivity investigation on the fog-haze area to $PM_{2.5}$ concentration. (a) Simulated fog-haze spatial distributions with varying $PM_{2.5}$ levels at 5 am, Feb. 9th, 2020: (i) original, (ii) 80%, (iii) 60%, and (iv) 40% original concentrations. (b) Population density in the study domain. (c) Time series of the hourly fog-haze area in Feb. 2020 by varying $PM_{2.5}$ concentrations in the study domain. (d) The cumulative probability of observed fog-haze area in Feb. and Jul. 2020 (the dots), with arrows showing the direction of simulated $PM_{2.5}$ variation, and (i) the simulation with original, 40%, 60% and 80% of winter $PM_{2.5}$ concentrations (the grey lines), and (ii) the simulation with original and 250% of summer $PM_{2.5}$ concentrations (the red lines). (e) Simulated response of the mean fog-haze area and population exposure to $PM_{2.5}$ reduction.

The cumulative probability distribution function (CDF) of fog-haze area in the study region demonstrates the consistency between model simulation and observation (Fig. 6d). The mean fog-haze area (50% CDF) is 9799 and 828 km^2 for Feb. and Jul., respectively. Since the observed mean summer-to-winter $PM_{2.5}$ ratio is approximately 0.42 (Fig. S3), reducing wintertime $PM_{2.5}$ concentrations to 40% can simulate the summer-like aerosol conditions (Fig. 6d (i)), and the resulting winter simulation curve (gray line) closely aligns with the observed summer distribution (red dots). Conversely, increasing summer $PM_{2.5}$ to 250% can allow the summer simulation to align with the observed winter distribution (black dots) (Fig. 6d(ii)). These results provide compelling evidence that the higher frequency of fog-haze events in winter is primarily driven by the elevated anthropogenic pollution levels. High aerosol loading can involve intense competition for available water vapor among a high number of cloud condensation nuclei (CCN), which can lead to numerous small droplets (Twomey, 1977b), creating much larger droplet surface area, and efficiently scattering light. This can form optically dense fog-haze rather than clean fog (Jia et al., 2026). In addition, the high moisture can promote the hygroscopic growth of aerosols and aqueous reactions for secondary aerosol formation, resulting in positive feedback in elevating $PM_{2.5}$ concentration (Peng et al., 2021; Zhong et al., 2018). By reducing $PM_{2.5}$ concentration, our experiments simulate a cleaner environment with fewer CCN. This results in the formation of fewer fog droplets and a shift from an aerosol-dominated event to a pure fog event, which is consistently demonstrated by the corresponding increase in pure fog coverage and occurrence probability under reduced $PM_{2.5}$ scenarios (Fig. S4).

4.5 Co-benefit evaluation of visibility improvement and human health by reducing $PM_{2.5}$

Fog-haze can exert adverse effects on human health, as intensive aqueous-phase processing facilitates the formation of water-soluble secondary aerosols (Wang et al., 2020). These soluble fractions exhibit enhanced bioavailability, allowing them to more effectively penetrate the blood-air barrier and trigger systemic toxicity (Miller et al., 2017; Pope and Dockery, 2006). Consequently, the synergistic interplay between high aerosol loading and elevated humidity amplifies the pathological burden, based on which the population exposure to fog-haze is analysed.

The sensitivity experiment above establishes the relationship between $PM_{2.5}$ abatement and the mitigation of winter fog-haze, thereby providing a foundation for policy assessment. Figure 6e quantifies the nonlinear response of $PM_{2.5}$ reduction on fog-haze area and its population exposure. With $PM_{2.5}$ reducing from original levels (100%) to 80%, the mean fog-haze area declined by 42% (black line in Fig. 6e), but the population exposure to fog-haze only reduced by 15% (red line in Fig. 6e). Further reduction of $PM_{2.5}$ largely reduced the fog-haze area; however, the reduction of population exposure showed only moderate effects, which tends to be effective only when $PM_{2.5}$ is reduced to levels below 60% of the original. This leads to a less steep gradient of reduction against $PM_{2.5}$ reduction for population exposure than the fog-haze area (the pink and grey lines in Fig. 6e).

The less effective elimination of population exposure than the fog-haze area itself is because the reduction of $PM_{2.5}$ firstly causes the elimination of fog-haze in regions with lower population density and less anthropogenic emissions. A further reduction of $PM_{2.5}$ is required to effectively reduce its population exposure, where the fog-haze is mainly controlled by regions with large anthropogenic emissions. Figure 6e gives this most effective stage is when $PM_{2.5}$ reduction is beyond 40%, by which the population exposure can be further decreased by 18% with 10% reduction in $PM_{2.5}$. After that, the elimination of population exposure can be more effective than the fog-haze area.

By identifying the intensity and regional distribution of LVEs, including unpolluted fog, polluted fog-haze, and sea fog using a machine-learning method, we are able to investigate the nonlinear relationships among pollution, visibility, and human health. High concentrations of aerosols can increase atmospheric stability and moisture, creating self-sustaining feedback loops that maintain the fog-haze (Wu et al., 2019; Yang et al., 2020). Effective visibility improvement only occurs when $PM_{2.5}$ concentration is reduced below the critical threshold required to break these feedbacks. Reductions in $PM_{2.5}$ lead to a prompt decrease in fog-haze coverage, but only over 40% reduction can effectively lower the population-weighted exposure. The results here give insights for policy implementation that the initial $PM_{2.5}$ reduction can be effective in controlling fog-haze areas, but further regulation is required to reduce the health risk for the population-dense cities. Beyond the threshold as identified here, co-benefits of visibility increase and health improvement can be achieved. Our quantitative LVE identification framework provides an advanced policy tool that can be further developed to guide transportation safety, health risk, and economic analysis.

5 Conclusion

This study developed and validated a deep learning-based frameworkthat couples high-frequency geostationary satellite observations (FY-4A), meteorological reanalysis (ERA5), and ground-based $PM_{2.5}$ measurements to accurately identify and quantify all-weather low-visibility events (LVEs) over eastern China. Anchored by ground-station visibility data as the target truth, the framework achieved an identification accuracy exceeding 90%. Crucially, by integrating $PM_{2.5}$ data, the model successfully disentangled the microphysical pathways of different LVEs, solving a persistent challenge in remote sensing over complex terrestrial and coastal environments.

Beyond accurate classification, this quantitative framework revealed a non-linear response of fog-haze events to $PM_{2.5}$ mitigation. Because initial emission controls primarily clear fog-haze in peripheral areas, moderate $PM_{2.5}$ reductions fail to proportionately alleviate population exposure. We identified a critical mitigation threshold indicating that $PM_{2.5}$ concentrations must be decreased by more than 40% to break the vicious cycle where accumulated aerosols stabilize the lower atmosphere and trap further pollution in densely populated urban cores.This explicitly underscores that deep, sustained emission cuts are necessary to achieve synchronized co-benefits for both urban visibility and public health.

Supplement

Supporting information, including data preprocessing and standardization, network architecture and attention mechanisms, hybrid loss function definition, and model training configuration (Texts S1–S4), illustration of the study domain and sampling method (Fig. S1), schematic of the CNN model configuration (Fig. S2), seasonal spatial patterns of $PM_{2.5}$ concentration (Fig. S3); seasonal responses of simulated fog and haze area to $PM_{2.5}$ concentration (Fig. S4) and summary of data sources, model performance metrics, and comparison with baseline models (Tables S1–S3)

Author contributions

Dantong Liu: Conceptualization, Methodology, Resources, Project administration, Funding acquisition, Supervision, Writing - original draft, Writing - review & editing. **Yuting Liang:** Conceptualization, Methodology, Software, Validation, Formal analysis, Investigation, Visualization, Writing - original draft, Writing - review & editing. **Shitong Zhao:** Investigation, Data curation, Writing - review & editing. **Changhao Wu:** Resources, Software, Investigation, Data curation, Writing - review & editing. **Li Yi:** Formal analysis, Validation, Writing - review & editing. **Xingcan Jia:** Methodology, Formal analysis, Validation, Writing - review & editing.

Competing interests

Dantong Liu is an editor of ACP.

Financial support

This work was supported by Science Fund for Distinguished Young Scholars of Zhejiang Province (LR24D050001).

Data availability

The ECMWF global meteorological reanalysis data are available from the Copernicus Climate Change Service (C3S) Climate Data Store (https://cds.climate.copernicus.eu/cdsapp#!/dataset/reanalysis-era5-single-levels). The FY-4A satellite data are available at the National Satellite Meteorological Center (NSMC) data portal (http://data.nsmc.org.cn/DataPortal/cn/data/detail.html). The hourly $PM_{2.5}$ measurements are available from the China National Environmental Monitoring Centre (CNEMC, http://air.cnemc.cn:18007/). The ground-based visibility observation data are sourced from the U.S. National Climatic Data Center (NCDC/NOAA, ftp://ftp.ncdc.noaa.gov/pub/data/noaa/isd-lite/). The annual population distribution data (2020) is available at the WorldPop website (https://www.worldpop.org/).

References

An, Z., Huang, R.-J., Zhang, R., Tie, X., Li, G., Cao, J., Zhou, W., Shi, Z., Han, Y., Gu, Z., and Ji, Y.: Severe haze in northern China: a synergy of anthropogenic emissions and atmospheric processes, Proc. Natl. Acad. Sci., 116, 8657–8666, https://doi.org/10.1073/pnas.1900125116, 2019.

Guide to Instruments and Methods of Observation (WMO-No. 8): https://community.wmo.int/site/knowledge-hub/programmes-and-initiatives/instruments-and-methods-of-observation-programme-imop/guide-instruments-and-methods-of-observation-wmo-no-8-0, last access: 10 June 2026.

Anthis, A. I. and Cracknell, A. P.: Use of satellite images for fog detection (AVHRR) and forecast of fog dissipation (METEOSAT) over lowland thessalia, hellas, Int. J. Remote Sens., 20, 1107–1124, https://doi.org/10.1080/014311699212876, 1999.

Cermak, J. and Bendix, J.: A novel approach to fog/low stratus detection using meteosat 8 data, Atmos. Res., 87, 279–292, https://doi.org/10.1016/j.atmosres.2007.11.009, 2008.

Ellrod, G. P.: Advances in the detection and analysis of fog at night using GOES multispectral infrared imagery, Weather Forecasting, 10, 606–619, https://doi.org/10.1175/1520-0434(1995)010%3C0606:AITDAA%3E2.0.CO;2, 1995.

Eyre, J. R., Brownscombe, J. L., and Allam, R. J.: Detection of fog at night using advanced very high resolution radiometer (AVHRR) imagery, Detect. fog night using Adv. Very High Resolut. Radiom. (AVHRR) imag., 113, 266–271, 1984.

Gultepe, I., Tardif, R., Michaelides, S. C., Cermak, J., Bott, A., Bendix, J., Müller, M. D., Pagowski, M., Hansen, B., Ellrod, G., Jacobs, W., Toth, G., and Cober, S. G.: Fog research: A review of past achievements and future perspectives, Pure Appl. Geophys., 164, 1121–1159, https://doi.org/10.1007/s00024-007-0211-x, 2007.

Hersbach, H., Bell, B., Berrisford, P., Hirahara, S., Horányi, A., Muñoz-Sabater, J., Nicolas, J., Peubey, C., Radu, R., Schepers, D., Simmons, A., Soci, C., Abdalla, S., Abellan, X., Balsamo, G., Bechtold, P., Biavati, G., Bidlot, J., Bonavita, M., Chiara, G. D., Dahlgren, P., Dee, D., Diamantakis, M., Dragani, R., Flemming, J., Forbes, R., Fuentes, M., Geer, A., Haimberger, L., Healy, S., Hogan, R. J., Hólm, E., Janisková, M., Keeley, S., Laloyaux, P., Lopez, P., Lupu, C., Radnoti, G., Rosnay, P. de, Rozum, I., Vamborg, F., Villaume, S., and Thépaut, J.-N.: The ERA5 global reanalysis, https://doi.org/10.1002/qj.3803, n.d.

Hu, J., Shen, L., and Sun, G.: Squeeze-and-excitation networks, Proceedings of the IEEE Conference on Computer Vision and Pattern Recognition, 7132–7141, 2018.

Huang, Y., Wu, M., Guo, J., Zhang, C., and Xu, M.: A correlation context-driven method for sea fog detection in meteorological satellite imagery, IEEE Geosci. Remote Sens. Lett., 19, 1–5, https://doi.org/10.1109/LGRS.2021.3095731, 2022.

Hunt, G. E.: Radiative properties of terrestrial clouds at visible and infra-red thermal window wavelengths, https://doi.org/10.1002/qj.49709942013, n.d.

Hutchison, K. D., Iisager, B. D., Kopp, T. J., and Jackson, J. M.: Distinguishing aerosols from clouds in global, multispectral satellite data with automated cloud classification algorithms, J. Atmos. Oceanic Technol., 25, 501–518, https://doi.org/10.1175/2007JTECHA1004.1, 2008.

Ioffe, S. and Szegedy, C.: Batch normalization: accelerating deep network training by reducing internal covariate shift, in: Proceedings of the 32nd International Conference on Machine

Learning, International Conference on Machine Learning, shortConferenceName: ICML, 448–456, 2015.

Israël, H. and Kasten, F.: KOSCHMIEDERs Theorie der horizontalen Sichtweite, in: Die Sichtweite im Nebel und die Möglichkeiten ihrer künstlichen Beeinflussung, VS Verlag für Sozialwissenschaften, Wiesbaden, 7–10, https://doi.org/10.1007/978-3-663-04661-5_2, 1959.

Jeon, H.-K., Kim, S., Edwin, J., and Yang, C.-S.: Sea fog identification from GOCI images using CNN transfer learning models, Electronics, 9, 311, https://doi.org/10.3390/electronics9020311, 2020.

Jia, X., Lu, C., Liao, Z., Tian, P., Wang, Y., Wang, F., Yang, S., Dou, Y., Liu, X., and Liu, Y.: Comprehensive analysis of the relative dispersion of droplet-size distributions and their relationships to key physical fog processes under different aerosol conditions and evolutionary stages, Adv. Atmos. Sci., 43, 861–873, https://doi.org/10.1007/s00376-025-4228-9, 2026.

Koračin, D., Dorman, C. E., Lewis, J. M., Hudson, J. G., Wilcox, E. M., and Torregrosa, A.: Marine fog: a review, Atmos. Res., 143, 142–175, https://doi.org/10.1016/j.atmosres.2013.12.012, 2014.

Koschmieder, H.: Theorie der horizontalen Sichtweite, Beiträge zur Physik der freien Atmosphäre, 12, 33–53, 1924.

Krizhevsky, A., Sutskever, I., and Hinton, G. E.: ImageNet classification with deep convolutional neural networks, in: Advances in Neural Information Processing Systems, 2012.

Lee, T. F., Turk, F. J., and Richardson, K.: Stratus and fog products using GOES-8–9 3.9-µm data, Weather Forecasting, 12, 664–677, https://doi.org/10.1175/1520-0434(1997)012%3C0664:SAFPUG%3E2.0.CO;2, 1997.

Li, Z., Guo, J., Ding, A., Liao, H., Liu, J., Sun, Y., Wang, T., Xue, H., Zhang, H., and Zhu, B.: Aerosol and boundary-layer interactions and impact on air quality, Natl. Sci. Rev., 4, 810–833, https://doi.org/10.1093/nsr/nwx117, 2017.

Lin, T.-Y., Goyal, P., Girshick, R., He, K., and Dollar, P.: Focal loss for dense object detection, Proceedings of the IEEE International Conference on Computer Vision, 2980–2988, 2017.

Liu, D. Y., Yan, W. L., Yang, J., Pu, M. J., Niu, S. J., and Li, Z. H.: A study of the physical processes of an advection fog boundary layer, Boundary Layer Meteorol., 158, 125–138, https://doi.org/10.1007/s10546-015-0076-y, 2016.

Liu, Y. and Daum, P. H.: Indirect warming effect from dispersion forcing, Nature, 419, 580–581, https://doi.org/10.1038/419580a, 2002.

Lyu, R., Wang, Y., Peng, Y., Gao, W., Yang, H., Tan, X., He, Q., Cheng, T., and Zhang, R.: Long-term variation characteristics and influencing factors of low-visibility events on the coast of China, Atmos. Res., 257, 105583, https://doi.org/10.1016/j.atmosres.2021.105583, 2021.

Mazoyer, M., Burnet, F., Denjean, C., Roberts, G. C., Haeffelin, M., Dupont, J.-C., and Elias, T.: Experimental study of the aerosol impact on fog microphysics, Atmos. Chem. Phys., 19, 4323–4344, https://doi.org/10.5194/acp-19-4323-2019, 2019.

Miller, M. R., Raftis, J. B., Langrish, J. P., McLean, S. G., Samutrtai, P., Connell, S. P., Wilson, S., Vesey, A. T., Fokkens, P. H. B., Boere, A. J. F., Krystek, P., Campbell, C. J., Hadoke, P.

W. F., Donaldson, K., Cassee, F. R., Newby, D. E., Duffin, R., and Mills, N. L.: Inhaled nanoparticles accumulate at sites of vascular disease, ACS Nano, 11, 4542–4552, https://doi.org/10.1021/acsnano.6b08551, 2017.

Milletari, F., Navab, N., and Ahmadi, S.-A.: V-net: fully convolutional neural networks for volumetric medical image segmentation, in: 2016 Fourth International Conference on 3D Vision (3DV), 2016 Fourth International Conference on 3D Vision (3DV), 565–571, https://doi.org/10.1109/3DV.2016.79, 2016.

Niu, F., Li, Z., Li, C., Lee, K.-H., and Wang, M.: Increase of wintertime fog in China: Potential impacts of weakening of the eastern asian monsoon circulation and increasing aerosol loading, J. Geophys. Res.: Atmos., 115, https://doi.org/10.1029/2009JD013484, 2010.

Pauli, E., Andersen, H., Bendix, J., Cermak, J., and Egli, S.: Determinants of fog and low stratus occurrence in continental central europe – a quantitative satellite-based evaluation, J. Hydrol., 591, 125451, https://doi.org/10.1016/j.jhydrol.2020.125451, 2020.

Peng, J., Hu, M., Shang, D., Wu, Z., Du, Z., Tan, T., Wang, Y., Zhang, F., and Zhang, R.: Explosive secondary aerosol formation during severe haze in the north China plain, Environ. Sci. Technol., 55, 2189–2207, https://doi.org/10.1021/acs.est.0c07204, 2021.

Pope, C. A. and Dockery, D. W.: Health effects of fine particulate air pollution: lines that connect, J. Air Waste Manage. Assoc., 56, 709–742, https://doi.org/10.1080/10473289.2006.10464485, 2006.

RenHe, Z., Li, Q., and Zhang, R.: Meteorological conditions for the persistent severe fog and haze event over eastern China in January 2013, Sci. China Earth Sci., 57, 26–35, https://doi.org/10.1007/s11430-013-4774-3, 2014.

Roach, W. T., Brown, R., Caughey, S. J., Garland, J. A., and Readings, C. J.: The physics of radiation fog: I – a field study, https://doi.org/10.1002/qj.49710243204, n.d.

Shin, D. and Kim, J.-H.: A new application of unsupervised learning to nighttime sea fog detection, Asia-Pac. J. Atmos. Sci., 54, 527–544, https://doi.org/10.1007/s13143-018-0050-y, 2018.

Twomey, S.: The influence of pollution on the shortwave albedo of clouds, J. Atmos. Sci., 34, 1149–1152, https://doi.org/10.1175/1520-0469(1977)034%3C1149:TIOPOT%3E2.0.CO;2, 1977a.

Twomey, S.: The influence of pollution on the shortwave albedo of clouds, J. Atmos. Sci., 34, 1149–1152, https://doi.org/10.1175/1520-0469(1977)034%3C1149:TIOPOT%3E2.0.CO;2, 1977b.

Integrated science assessment (ISA) for particulate matter: https://www.epa.gov/isa/integrated-science-assessment-isa-particulate-matter, last access: 25 January 2026.

Regional haze program: https://www.epa.gov/visibility/regional-haze-program, last access: 25 January 2026.

Wang, J., Li, J., Ye, J., Zhao, J., Wu, Y., Hu, J., Liu, D., Nie, D., Shen, F., Huang, X., Huang, D. D., Ji, D., Sun, X., Xu, W., Guo, J., Song, S., Qin, Y., Liu, P., Turner, J. R., Lee, H. C., Hwang, S., Liao, H., Martin, S. T., Zhang, Q., Chen, M., Sun, Y., Ge, X., and Jacob, D. J.: Fast sulfate formation from oxidation of SO2 by NO2 and HONO observed in Beijing haze, Nat. Commun., 11, 2844, https://doi.org/10.1038/s41467-020-16683-x, 2020.

Wang, Q., Yamaguchi, R. T., Kalogiros, J. A., Daniels, Z., Alappattu, D. P., Jonsson, H., Alvarenga, O., Olson, A., Wauer, B. J., Ortiz-Suslow, D. G., and Fernando, H. J.:

Microphysics and Optical Attenuation in Fog: Observations from Two Coastal Sites, Boundary-Layer Meteorol, 181, 267–292, https://doi.org/10.1007/s10546-021-00675-5, 2021.

Wei, J., Li, Z., Pinker, R. T., Wang, J., Sun, L., Xue, W., Li, R., and Cribb, M.: Himawari-8-derived diurnal variations in ground-level $PM_{2.5}$ pollution across china using the fast space-time light gradient boosting machine (LightGBM), Atmos. Chem. Phys., 21, 7863–7880, https://doi.org/10.5194/acp-21-7863-2021, 2021.

Woo, S., Park, J., Lee, J.-Y., and Kweon, I. S.: CBAM: convolutional block attention module, Proceedings of the European Conference on Computer Vision (ECCV), 3–19, 2018.

World Meteorological Organization (WMO): Guide to Instruments and Methods of Observation (WMO-No. 8), 2024 edition, Volume I, Chapter 9: Measurement of visibility, World Meteorological Organization, Geneva, Switzerland, 2024.

Wu, D., Lu, B., Zhang, T., and Yan, F.: A method of detecting sea fogs using CALIOP data and its application to improve MODIS-based sea fog detection, J. Quant. Spectrosc. Radiat. Transfer, 153, 88–94, https://doi.org/10.1016/j.jqsrt.2014.09.021, 2015.

Wu, J., Bei, N., Hu, B., Liu, S., Zhou, M., Wang, Q., Li, X., Liu, L., Feng, T., Liu, Z., Wang, Y., Cao, J., Tie, X., Wang, J., Molina, L. T., and Li, G.: Aerosol–radiation feedback deteriorates the wintertime haze in the north China plain, Atmos. Chem. Phys., 19, 8703–8719, https://doi.org/10.5194/acp-19-8703-2019, 2019.

Wu, Y., Liu, Q., Liu, D., Tian, P., Xu, W., Wang, J., Hu, K., Li, S., Jiang, X., Wang, F., Huang, M., Ding, D., Yu, C., and Hu, D.: Enhanced formation of nitrogenous organic aerosols and brown carbon after aging in the planetary boundary layer, npj Clim. Atmos. Sci., 7, 179, https://doi.org/10.1038/s41612-024-00726-x, 2024.

Xu, M., Chen, K., Guo, H., Huang, Y., Wu, M., Shi, Z., Zhang, C., and Guo, J.: MFogHub: bridging multi-regional and multi-satellite data for global marine fog detection and forecasting, n.d.

Yang, C., Clarke, K., Shekhar, S., and Tao, C. V.: Big spatiotemporal data analytics: a research and innovation frontier, Int. J. Geogr. Inf. Sci., 34, 1075–1088, https://doi.org/10.1080/13658816.2019.1698743, 2020.

Yang, J., Zhang, Z., Wei, C., Lu, F., and Guo, Q.: Introducing the new generation of chinese geostationary weather satellites, fengyun-4, https://doi.org/10.1175/BAMS-D-16-0065.1, 2017.

Zhang, Q., Streets, D. G., Carmichael, G. R., He, K. B., Huo, H., Kannari, A., Klimont, Z., Park, I. S., Reddy, S., Fu, J. S., Chen, D., Duan, L., Lei, Y., Wang, L. T., and Yao, Z. L.: Asian emissions in 2006 for the NASA INTEX-B mission, Atmos. Chem. Phys., 9, 5131–5153, https://doi.org/10.5194/acp-9-5131-2009, 2009a.

Zhang, S. and Yi, L.: A comprehensive dynamic threshold algorithm for daytime sea fog retrieval over the chinese adjacent seas, Pure Appl. Geophys., 170, 1931–1944, https://doi.org/10.1007/s00024-013-0641-6, 2013.

Zhang, S.-P., Xie, S.-P., Liu, Q.-Y., Yang, Y.-Q., Wang, X.-G., and Ren, Z.-P.: Seasonal variations of yellow sea fog: observations and mechanisms, J. Clim., 22, 6758–6772, https://doi.org/10.1175/2009JCLI2806.1, 2009b.

Zhang, X. Y., Wang, Y. Q., Niu, T., Zhang, X. C., Gong, S. L., Zhang, Y. M., and Sun, J. Y.: Atmospheric aerosol compositions in China: spatial/temporal variability, chemical signature, regional haze distribution and comparisons with global aerosols, Atmos. Chem. Phys., 12, 779–799, https://doi.org/10.5194/acp-12-779-2012, 2012.

Zhong, J., Zhang, X., Dong, Y., Wang, Y., Liu, C., Wang, J., Zhang, Y., and Che, H.: Feedback effects of boundary-layer meteorological factors on cumulative explosive growth of $PM_{2.5}$ during winter heavy pollution episodes in Beijing from 2013 to 2016, Atmos. Chem. Phys., 18, 247–258, https://doi.org/10.5194/acp-18-247-2018, 2018.